ADVANCED ENERGY MATERIALS
www.advenergymat.de

High-Performing All-Solid-State Sodium-Ion Batteries Enabled by the Presodiation of Hard Carbon

*Jin An Sam Oh, Grayson Deysher, Phillip Ridley, Yu-Ting Chen, Diyi Cheng, Ashley Cronk, So-Yeon Ham, Darren H.S. Tan, Jihyun Jang, Long Hoang Bao Nguyen, and Ying Shirley Meng**

All-solid-state sodium ion batteries (AS^3iBs) are highly sought after for stationary energy storage systems due to their suitable safety and stability over a wide temperature range. Hard carbon (HC), which is low cost, exhibits a low redox potential, and a high capacity, is integral to achieve a practical large-scale sodium-ion battery. However, the energy density of the battery utilizing this anode material is hampered by its low initial Coulombic efficiency (ICE). Herein, two strategies, namely i) additional pyrolysis and ii) presodiation by thermal decomposition of $NaBH_4$, are explored to improve the ICE of pristine HC. Raman spectroscopy, X-ray photoelectron spectroscopy, and electrochemical characterizations elucidate that the thermal treatment increases the C_{sp2} content in the HC structure, while the presodiation supplies the sodium to occupy the intrinsic irreversible sites. Consequently, presodiated HC exhibits an outstanding ICE (>99%) compared to the thermally treated (90%) or pristine HC (83%) in half-cell configurations. More importantly, AS^3iB using presodiated HC and $NaCrO_2$ as the anode and cathode, respectively, exhibits a high ICE of 92% and an initial discharge energy density of 294 Wh $kg^{-1}_{cathode}$.

1. Introduction

Recent global electrification efforts have resulted in the price of lithium resources trending upward and, thus, the cost of lithium-ion batteries (LIBs) to increase at an unprecedented rate.[1] Due to the abundance and low cost of sodium-based materials, sodium-ion batteries (SIBs) can play an important role as a complementary system, especially in large-scale stationary energy storage systems and low-end vehicles.[2] Conventional LIBs and SIBs use organic liquid electrolytes which then pose leakage risks, narrow temperature windows for operation, and are also flammable. Replacing the separator and liquid electrolyte with an inorganic solid-state electrolyte (SSE) can effectively mitigate the limitations of conventional batteries. In all-solid-state sodium ion batteries (AS^3iBs), the electrochemical stability of the SSE with the electrode determines the type of interface.[3] A thermodynamically stable interface between the SSE and the electrode is preferred to eradicate sodium loss due to formation of solid electrolyte interphase (SEI). Recently, $Na_4(B_{10}H_{10})(B_{12}H_{12})$, or NBH, SSE has been reported to have a high ionic conductivity around 1 mS cm^{-1}, which is very similar to common liquid electrolytes, allowing these AS^3iBs to operate at room temperature with minimal overpotential.[4] Moreover, it is electrochemically stable with metallic sodium allowing for a

J. A. S. Oh, P. Ridley, D. Cheng, D. H. Tan, J. Jang[+], L. H. B. Nguyen, Y. S. Meng
Department of NanoEngineering
University of California San Diego
La Jolla, CA 92093, USA
E-mail: shirleymeng@uchicago.edu

The ORCID identification number(s) for the author(s) of this article can be found under https://doi.org/10.1002/aenm.202300776

[+]Present address: Department of Chemistry, Sogang University, 35 Baekbeom-ro, Mapo-gu, Seoul 04107, Republic Of South Korea

DOI: 10.1002/aenm.202300776

J. A. S. Oh
Institute of Materials Research and Engineering
Agency of Science, Technology, and Research (A*STAR)
Singapore 138634, Singapore

G. Deysher, Y.-T. Chen, A. Cronk, S.-Y. Ham
Program of Materials Science and Engineering
University of California San Diego
La Jolla, CA 92093, USA

Y. S. Meng
Pritzker School of Molecular Engineering
The University of Chicago
Chicago, IL 60637, USA

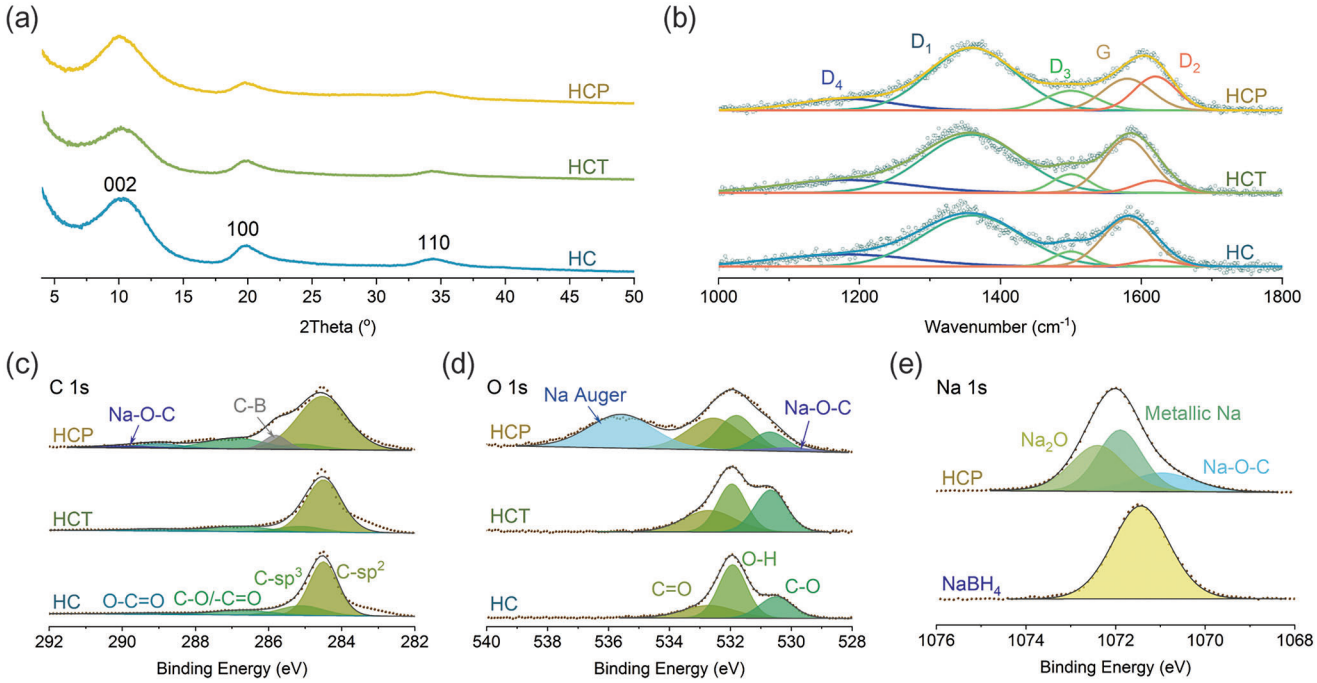

Figure 1. a) XRD patterns, b) Raman spectra, and high resolution XPS c) C 1s, and d) O 1s spectra of HC, HCT, and HCP, and e) comparison of XPS Na 1s spectra of HCP and as-received $NaBH_4$.

stable interface at low potential.[5] Thus, NBH is a promising SSE which can be paired with the anode in the AS^{3}iBs.

Although numerous alloy-based materials, such as Sn, Sb, and Ge,[6] have shown good potential as sodium anode materials, carbon-based materials are preferred for their environmental-friendliness, low cost, and low redox potentials. Hard carbon (HC), which consists of a low degree of graphitized carbon, has been shown to be a promising anode material for SIBs with a specific capacity of 250–300 mAh g^{-1}.[7] Furthermore, HC exhibits low redox potential (≈1 to 0.1 V vs Na/Na^+) that can theoretically enable high energy density batteries. However, the bottleneck that limits the application of HC in practical batteries is its low initial Coulombic efficiency (ICE), around 80–90% depending on the synthesis, mass loading, and electrolyte, which consume the available mobile ions inventory.[8] Moreover, the real-world battery configuration has the cathode providing the limited mobile sodium ions inventory suffers from poor reversible cell capacity due to the loss of Na inventory in irreversible capacities, hindering the commercial potential.[9] Particularly, the loss of sodium ions inventory in the initial cycles is primarily attributed to the formation of an SEI at the interface between HC and electrolyte.[10] In addition to SEI formation, functional groups or surface defects within the HC structure, which possess high binding energies with sodium ions, can also contribute to its low ICE.[11] The amount of such sodium irreversible sites can be greatly removed by optimizing pyrolysis temperature and duration to increase the graphitization or C_{sp2}:C_{sp3} ratio.[12] Nonetheless, these irreversible sites cannot be eliminated completely even with optimal synthesis conditions. To overcome the low ICE, presodiating the HC is one of the most promising methods to compensate for the loss of mobile sodium ions inventory during the initial cycles.[13] To date, presodiation has been achieved either electrochemically or chemically which inevitably creates an organic layer on the HC due to the decomposition of the organic electrolyte at the low potentials during presodiation.[9a,14]

In this study, two strategies are investigated to improve the ICE of the HC anode: 1) additional pyrolysis at 1000 °C and 2) presodiation by the thermal decomposition of $NaBH_4$ additive. The experimental results suggest that the additional pyrolysis increases the graphitization and, thus, the C_{sp2}:C_{sp3} ratio, while the thermal decomposition of $NaBH_4$ produces metallic sodium on the HC surfaces to compensate sodium loss. Consequently, the thermally treated HC has a slightly improved half-cell ICE, increasing from 83% to 90%, while presodiation enables an extremely high ICE of >99%. Electrochemical characterization and X-ray photoelectron spectroscopy (XPS) reveals that the irreversible sodium ions in the HC exist in the form of Na–O–C, which is an intrinsic sodium storage mechanism in HC structure. Last, AS^{3}iBs are assembled to demonstrate that the ICE can be increased from 75% to 92% and that the capacity retention is significantly higher by presodiating the HC.

2. Results and Discussion

The long-range structures of pristine hard carbon (HC), thermally treated hard carbon (HCT), and presodiated hard carbon (HCP) were investigated by X-ray diffraction (XRD). All three samples exhibited broad diffraction peaks (**Figure 1**a) indicating that all the samples have low crystallinity. **Table 1** summarizes the average interlayer spacing between graphene sheets (d_{002}), the average width of the order-layered nanodomains (L_a) and thickness (L_c) of the coherent domain, and the number of graphene sheets per stack (N) estimated by the Bragg's equation, Debye–Scherrer equation (Equations (1) and (2)), and the XRD profiles.[15] The

Table 1. Physical parameters of the hard carbon materials.

	d_{002} [Å]	L_a [nm]	L_c [nm]	Number of graphene layers [N]	I_D/I_G	A_{D4}/A_G
HC	3.90	3.54	1.11	3.84	1.14	0.71
HCT	3.85	3.56	1.19	4.09	1.07	0.64
HCP	4.02	3.39	1.16	3.90	1.17	0.72

estimated d_{002} of HC, HCT, and HCP were around 3.90, 3.85, and 4.02 Å, respectively, which are larger than that of graphite (≈3.34 Å) and will be favorable for sodium ions insertion.[15a,16] Compared to pristine HC, the HCT exhibited a slight expansion in the L_c and N which can be attributed to pyrolysis increasing the degree of graphitization.[12c,17] Interestingly, HCP exhibited a smallest L_a, and largest d_{002} indicating the size of the order-layered nanodomain decreased while a larger interlayer spacing between the graphitic layer. This is attributed to the thermal decomposition of $NaBH_4$ incorporating the boron atoms in the graphitic layer that disrupt the ordering of graphitic domain leading to a more disordered structure. Additionally, boron doping can alter the interlayer spacing by either reducing the van der Waals forces that hold the layers together or by inducting structural distortion.

$$L_{a/c} = \frac{K\lambda}{\beta_{a/c}\cos\theta_{a/c}} \quad (1)$$

$$N = \frac{L_c + d_{002}}{d_{002}} \quad (2)$$

where β is the full width at half-maximum of the XRD peak, λ is the wavelength of the X-ray used (λ_{Mo} = 0.071 nm), θ is the position of (002) and (100) peaks in XRD, and the corresponding K values of 0.89 and 1.84 for (002) and (100), respectively.[18]

The Raman spectra of HC, HCT, and HCP in Figure 1b have two characteristic peaks located at around 1345 and 1585 cm^{-1}, which are attributed to the C–C vibrational mode in the disordered (D-band) and graphitized (G-band) carbon structures, respectively. Thus, the I_D/I_G intensity ratio can provide an insight into the degree of disorder in the hard carbon structure. HCT possessed a lower I_D/I_G ratio compared to that of HC (1.07 vs 1.14), attributing to the removal of functional groups and the increase in the graphitization by the supplied thermal energy.[12c] HCP exhibited the highest I_D/I_G (1.17) which can be attributed to the incorporation of boron into the graphene layer during the presodiation. In order to better understand the structural evolution during pyrolysis and presodiation, the Raman spectra were deconvoluted into five peaks centering at 1180, 1360, 1500, 1585, and 1620 cm^{-1} corresponding to D4, D1, D3, G, and D2 bands, respectively.[12b,15b] The G band is ascribed to the ideal C–C vibrations in graphitic lattice with E_{2g}-symmetry, while D1 and D2 bands are referred to C–C vibrations in disordered graphitic lattices with A_{1g}- and E_{2g}-symmetries, respectively. The D3 band corresponds to the amorphous carbon and D4 is mainly due to ionic impurities.[19] Thus, the ratio of carbon bonded to functional groups on the HC surface to the amount bonded to the graphitic layer can be estimated from the area ratio of D4 and G (A_{D4}/A_G). By this estimation, HCT had the lowest A_{D4}/A_G ratio while HCP exhibited the highest A_{D4}/A_G ratio agreeing with the I_D/I_G ratio (Table 1).

XPS was conducted to reveal the carbon, oxygen, and sodium electronic states in HC, HCT, and HCP. The high-resolution C 1s spectra in Figure 1c can be resolved into four components with center at 284.5, 285.2, 286.7, and 289.1 eV corresponding to C_{sp2}, C_{sp3}, C–O/–C=O, and O–C=O.[12a] The C_{sp2}:C_{sp3} ratio of HC and HCT are 3.61 and 7.49, respectively, indicating the formation of a highly ordered carbon structure, or removal of the defects in the carbon domains, during the thermal treatment. Interestingly, both HC and HCT exhibited a decreasing C_{sp2}:C_{sp3} ratio in the depth profile (Figure S1a,b, Supporting Information), suggesting that the defects in the inner part cannot be dissociated out of the structure with the additional pyrolysis. Comparing with HC and HCT, HCP exhibited two additional peaks centered at 285.7 and 290.0 eV attributing to C–B[20] and Na–O–C,[21] respectively. The boron binding energy shifted from 187.2 and 191.5 eV in $NaBH_4$ to 187.8 eV in HCP (Figure S1c, Supporting Information), which can be assigned to C–B,[22] further affirming that the boron has been doped into the hard carbon structure during the thermal presodiation. The Na–O–C binding is supported with the additional peak at 530.4 eV for HCP in O 1s (Figure 1d) and 1070.9 eV in Na 1s XPS spectra (Figure 1e).[9a,14b,c] Besides Na–O–C, HCP also had two Na 1s XPS peaks around 1071.9 and 1072.5 attributing to metallic Na and Na_2O, respectively.[23] The presence of Na_2O signals is likely due to the oxidation of metallic sodium during sample transfer.

Scanning electron microscopy (SEM) images of the pristine HC, HCT, and HCP (**Figures 2**a to 2f, respectively) show similar particle morphology and size (≈10–30 µm), indicating that neither thermal treatment nor presodiation causes any noticeable change in particle size. At higher magnification, the surfaces of HC and HCT were smooth while HCP appeared to be textured. This is likely due to the deposition of decomposed products from $NaBH_4$ on the HCP surface. Furthermore, the scanning transmission electron microscopy with energy dispersive X-ray spectroscopy (STEM-EDX) image reveals strong Na signals, detecting that a significant amount of sodium was deposited on the surface of the HCP particles (Figure 2g). High-resolution transmission electron microscopy (HRTEM) images reveal that all the hard carbon particles consist of curved and randomly orientated graphene layers (Figure S2, Supporting Information), which agrees with the "house of cards" model of hard carbon.[24] Furthermore, the inset selected area electron diffraction patterns exhibit dispersed diffraction rings which supports the turbostratic and random stacking of graphene layers. Additionally, the diffraction fringes of the HC, HCT, and HCP correspond to an average d_{002}-spacing of 3.87, 3.72, and 3.92 Å, respectively.

The $Na_4(B_{10}H_{10})(B_{12}H_{12})$ (NBH) SSE, with the particle size of ≈5–10 µm (Figure S3a, Supporting Information), was used as the solid-state electrolyte in this study. The Nyquist plot in Figure S3b, Supporting Information, suggests that NBH has a room-temperature ionic conductivity of 1.8 mS cm^{-1} agreeing well with previous works.[5,25] The reduction stability at low potential of NBH was examined by cyclic voltammetry (CV) using a Na_9Sn_4|NBH|NBH+stainless-steel cell (Figure S3c, Supporting Information). The cell showed a strong reduction peak with an onset around 0 V versus Na/Na^+ that can be attributed to sodium

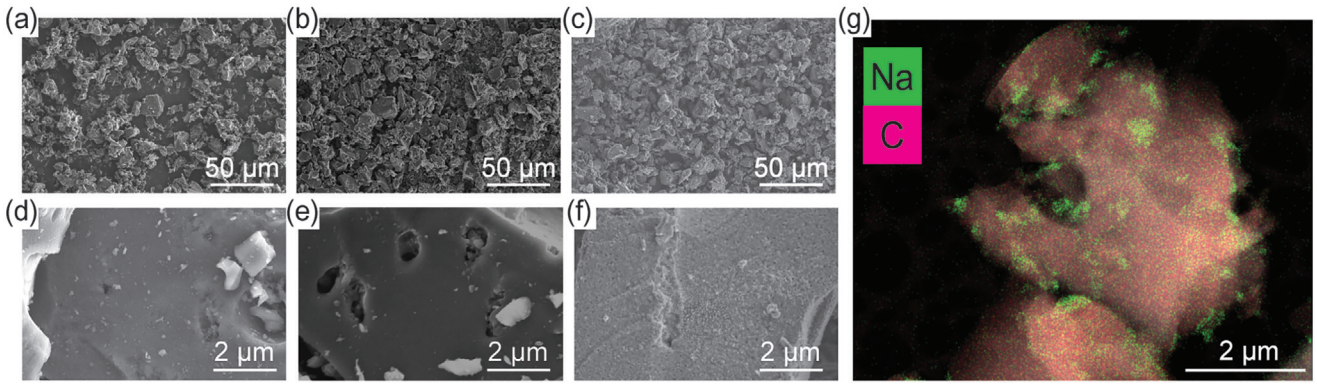

Figure 2. SEM images of a,d) HC, b,e) HCT, and c,f) HCP, respectively, and g) STEM-EDX of HCP

plating on the stainless-steel current collector. On the returning sweep, an oxidation peak that began at around 0.5 V versus Na/Na^+ can be ascribed to stripping of the deposited sodium. More importantly, there was no noticeable reductive current between the OCV and 0 V, which evidently demonstrated that NBH is highly stable at low potential and an interphase layer should not form electrochemically.[25] On the sidenote, an electrochemically stable interface would allow for a larger electrode/electrolyte surface contact area, which is necessary when using a composite electrode to enhance the sodium diffusion kinetics, without reducing the mobile sodium ions inventory.

The effect of charge transfer due to different amount of physical contact between the HC and SSE on the electrochemical performance was evaluated by assembling different weight ratio of HC:NBH composite (e.g., 100:0, 80:20, 70:30, and 60:40) in a half-cell configuration using Na_9Sn_4 as the counter electrode; the lower HC:NBH wt. ratio in the composite, the larger the electrolyte/electrode contact area is for ionic conduction. Galvanostatic (de)sodiation cycling was carried out to study the sodium storage mechanisms. Comparing the potential profiles, 100 wt.% HC exhibited a low potential "plateau" profile while composite HCs had a "slope" followed by low potential "plateau" profile (Figure S4a, Supporting Information). This hints different sodium storage mechanisms which can be attributed to the lack of ionic conduction path for electrochemical reactions. Consequently, the 100 wt% HC had an ICE of 43.0% while the composite anodes had an ICE of 83.5 to 84.9%. More importantly, the absolute irreversible capacity consistently around 43–46 mAh g^{-1} (or, 0.38–0.41 mAh cm^{-2}) supports that the HC/SSE interfaces are relatively stable, and formation of solid–electrolyte interface is improbable. Although all composite HC exhibited similar capacity at low current density, 70 wt.% HC delivered a highest normalized capacity at higher current density (Figure S4b, Supporting Information). Thus, an anode composite HC:NBH wt.% ratio of 70:30 was used for this study.

Figure 3a shows the Nyquist plots of the as-assembled HC, HCT, and HCP half-cells. All cells showed a high-frequency Z'-axis intercept followed by one semicircle (10^5–10^4 Hz), which can be attributed to the NBH resistance and electrode/electrolyte interface resistance, respectively, and a polarization tail.[26] HCP exhibited a smaller polarization tail in the low-frequency region compared to HC and HCT, which implies that the cell was at a different state-of-charge. This observation indicates that sodium was present within the HCP structure. Nevertheless, using the equivalent circuit (Figure 3a inset), all cells had similar total cell resistances (≈90–100 Ω cm^2), which includes the NBH and interface resistance, at the as-assembled state indicating no significant differences in the interfacial properties between different electrodes.

The potential response of the respective HC|NBH|Na_9Sn_4 half-cells (Figure 3b) was like those observed in liquid electrolytes,[21,27] with a slope at >0.15 V and a plateau between 0.15–0.02 V versus Na/Na^+ during sodiation. This implies that the HC has a similar sodium storage mechanism in a solid-state battery as in a liquid electrolyte battery. All cells delivered a sodiation capacity of around 260–280 mAh g^{-1} (or 2.25–2.40 mAh cm^{-2}), which is close to the capacity of HC reported in the liquid electrolyte battery, indicating a good utilization of the active material in the composite electrode. Upon desodiation, all cells delivered similar capacities of ≈245–255 mAh g^{-1}. Accordingly, HCP had the highest ICE of 99.6 ± 0.6%, followed by HCT (89.6 ± 0.9%), then HC (82.5 ± 0.6%). The corresponding dQ/dV profile in the first cycle showed only one pair of distinct (de)sodiation peaks near 0.06 and 0.26 V versus Na/Na^+ (Figure S5a, Supporting Information), which can be ascribed to the insertion and removal of sodium from the HC structure. Additionally, HCP had a significantly lower average open-circuit voltage (OCV) of 1.11 ± 0.05 V compared to pristine HC and HCT at 1.56 ± 0.11 and 1.60 ± 0.04 V versus Na/Na^+ (Figure 3c), respectively. This further affirms that HCP was at different state-of-charge following presodiation. Interestingly, the reversible capacities of HC and HCT in the subsequent cycle were relatively constant (≈245–255 mAh g^{-1}) and the Coulombic efficiencies were above 99% after the initial sodium loss during the first cycle. This observation suggests that the initial sodiation involved both reversible and irreversible sodium storage sites and only the reversible ones took part in the electrochemical reaction in subsequent cycles. In order to show that the deposited sodium on HCP is electrochemically active, the Na_9Sn_4||HCP half-cell was desodiated in the initial cycle (Figure S5b, Supporting Information). A desodiation capacity of 9.63 mAh g^{-1} and the subsequent cycle showed a Coulombic efficiency of 89.6%, which is close to HCT's efficiency. Intuitively, the supplemental sodium sources saturate all the irreversible sites in the initial sodiation and, thus, the sodium ions provided by the counter electrode is almost all completely reversible. To verify that the

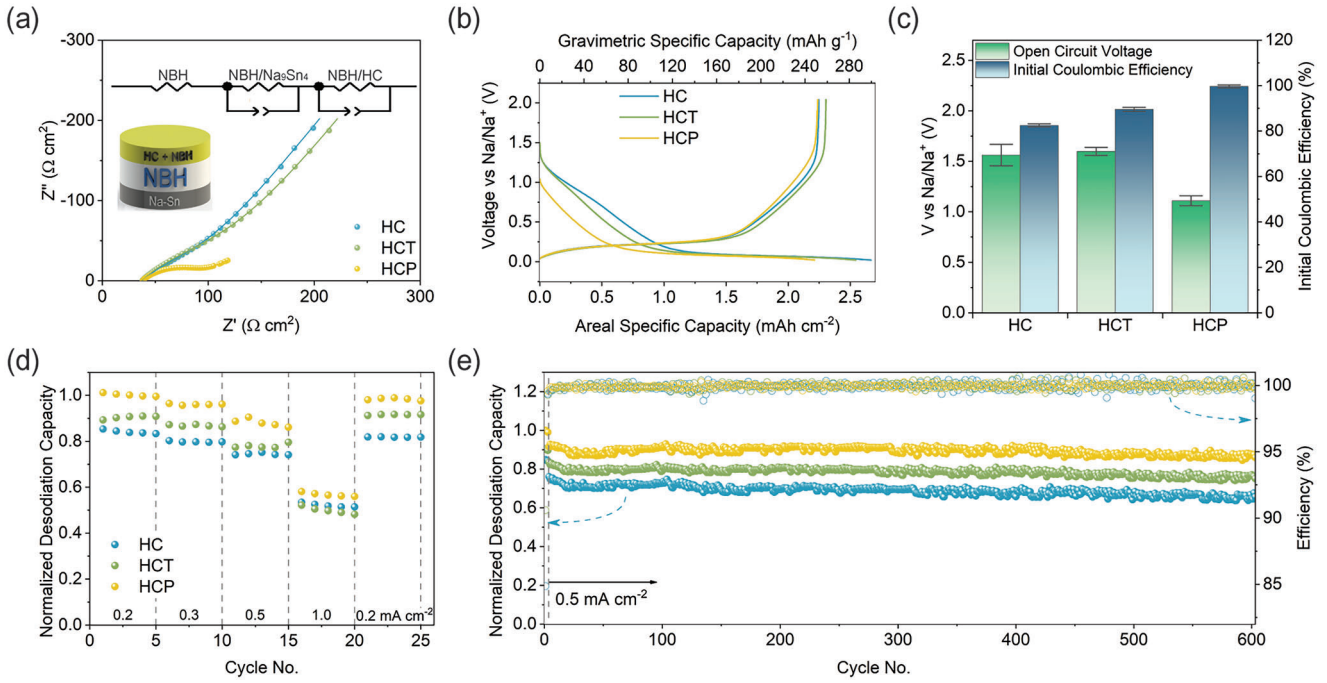

Figure 3. a) Nyquist plot of the pristine HC|NBH|Na_9Sn_4 half-cell, b) potential profile of HC at a current density of 0.2 mA cm^{-2}, c) OCV and ICE of HCs half-cells, d) potential profile of HCP at different current densities, d) reversible capacity of HCs at different current densities, and e) long-term cycling performance of half-cell at a current density of 0.5 mA cm^{-2}.

improvement of the ICE in HCP is due to the decomposition of $NaBH_4$ at high temperature, two samples were prepared; 1) HCT were thermally treated again under vacuum (e.g., HCT-T) and 2) HCT was physically mixed with $NaBH_4$ without heat treatment (HCP-NH). Both HCT-T and HCP-NH did not show significant improvement in the ICE (Figure S5c,d, Supporting Information). These further demonstrate that thermal decomposition of $NaBH_4$ is necessary to effectively nullify sodium loss due to the irreversible sodium sites present in HC.

The rate performance of HC, HCT, and HCP at 0.2. 0.3, 0.5, and 1.0 mA cm^{-2} current densities and the normalized capacity is given in Figure 3d. Accordingly, HCP delivered a higher normalized reversible capacity than HCT and HC at all current densities, which is attributed to its lower capacity loss in the initial cycle. All cells recovered their initial capacity when the current density returned to 0.2 mA cm^{-2}, indicating that the configuration is tolerant to higher current densities. The lower reversible capacity at higher current density can be attributed to sluggish electrochemical kinetics within the hard carbon and/or at the HC/NBH interface. The sodium storage reversibility of the HC, HCT, and HCP were investigated by repeated cycling at 0.2 mA cm^{-2} for 3 cycles followed by 0.5 mA cm^{-2} for 600 cycles (Figure S6a–c, Supporting Information). Although HCP exhibited a lower sodiation capacity of 245 mAh g^{-1} than HC and HCT (290 and 285 mAh g^{-1}, respectively) at 0.2 mA cm^{-2}, all cells had similar desodiation capacity of 245–260 mAh g^{-1}. Figure 3e shows the normalized desodiation capacity, the long-term galvanostatic cycling and the HCP cell delivered a higher normalized reversible capacity due the improved ICE. All cells had marginal capacity fading after 600 cycles at 0.5 mA cm^{-2} and an average Coulombic efficiency of 99.9%, which reflects that (de)sodiation within hard carbon structure is highly reversible.

To study the impact of supplemental sodium ions on the half-cell performance, hard carbons presodiated with excess capacity (e.g., HCP-x where $x = 20$, 40, and 60 mAh g^{-1}) were prepared by mixing different amounts of $NaBH_4$ with HC. The XRD profiles suggest that either no or low wt% secondary crystalized phase formation (Figure S7a, Supporting Information). Furthermore, compared to HCP with zero excess capacity in Figure 2g, HCP-60 exhibited a significantly stronger distribution of Na signals credited to more sodiation on the HC particles (**Figure 4**a). Due to the addition sodium in the HCP, the OCV of the assembled cells decreased from 1.11 to 0.80 V versus Na/Na^+ as more excess capacity from $NaBH_4$ was added to the mixture (Figure 4b). More importantly, the sodiation capacities from the counter electrode reduced while the desodiation capacities were consistently around 240–260 mAh g^{-1} (Figure S7b, Supporting Information). Therefore, the ICE of HCP increases with the amount of $NaBH_4$ added, while the capacities in the subsequent cycles were recovered to about 240–260 mAh g^{-1} (Figure S7c, Supporting Information). The dQ/dV plots of the HCP-x overlapped each other indicating that they exhibit a similar sodium storage mechanism (Figure 4c), as expected. However, the cells exhibited a lower excess capacity than the theoretical capacity provided by the thermal decomposition of $NaBH_4$ and such deviation increases with more $NaBH_4$ added. To investigate this, the amount of metallic Na was quantified by titration gas chromatography (TGC).[27b,28] The calculated capacity obtained via TGC deviates slightly from the electrochemical excess capacities suggesting formation of sodium compound reducing the active sodium inventory (Figure S7d,

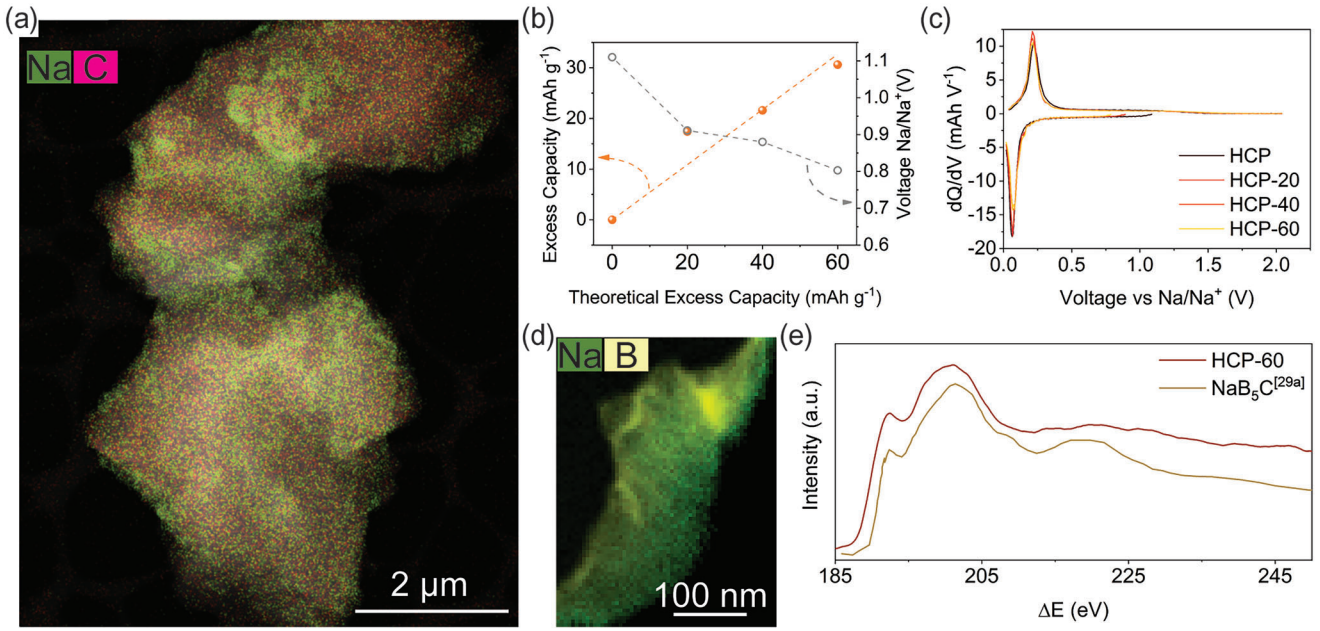

Figure 4. a) STEM-EDS mapping of HCP-60, b) excess capacity and OCV, c) dQ/dV plot of HCP-x, and EELS d) mapping and e) B K edge of HCP-60.

Supporting Information). The distribution of B and Na on the HCP-60 was verified by electron energy-loss spectroscopy (EELS) elemental mapping (Figure 4d and Figure S7e, Supporting Information). However, the EELS B K edge spectrum (Figure 4e) suggests that the thermal decomposition of $NaBH_4$ leads to the formation of a Na–B–C compound which has similar bonding as NaB_5C which has low sodium capacity reversibility.[29] As a result, the excess capacity is lower than the theoretical value. Nevertheless, it is still possible to presodiate the HC with excess capacity by adding more $NaBH_4$ and, thus, enabling the use of sodium-deficient cathode materials (e.g., $Na_{2/3}Ni_{1/3}Mn_{2/3}O_2$[30] and $Na_{0.6}[Li_{0.2}Mn_{0.8}]O_2$[31]) in a full-cell configurations and in full-cell configurations where SEI formation consumes a significant portion of the fixed Na inventory.

Given the electrochemical stability between HC and SSE, the HC and HCT still possessed an ICE <90% implies there were intrinsic irreversible sites in the structure. This is reflected by the OCV of all cells after one charge–discharge cycle which were around 1.15 V versus Na/Na^+, which is significantly lower than in the pristine state, indicating that they were at different state-of-charge. The HC and HCT cells were desodiated with a constant current constant voltage step, but negligible capacity could be recovered even at higher cut-off voltage (Figure S8a,b, Supporting Information). This suggests that the irreversible sodium ions were not limited by kinetics but rather were thermodynamically stable and irreversible due to the strong binding energy between the sodium ions and hard carbon. Nyquist plots of the HC, HCT, and HCP cells at the desodiated state during the 20 cycles at 0.2 mA cm^{-2} showed similar resistance, indicating no significant degradation or formation of a resistive interphase that occurred during cycling (Figure S8c, Supporting Information). The cyclic voltammograms of HC, HCT, and HCP cells exhibited one broad and one sharp redox pairs at 0.65/1.20 and 0.02/0.35 V versus Na/Na^+ (**Figure 5**a–c), respectively, which is simlar when using liquid electrolyte.[32] It is worthy to note that HC had a strong reduction peak at ≈0.65 V, which became weaker in subsequent cycles, while HCT also exhibited such changes but at a reduced scale. Interestingly, the metallic sodium on HCP that migrated into the irreversible sites was not detected in the CV, potentially due to the lower pristine OCV and reduction peak overlapped with the OCV, making it less obvious. Similar behavior was also observed in the dQ/dV profiles (Figure S9a–c, Supporting Information). Particularly, a weaker reduction peak in the subsequent cycles indicates the electrochemical reaction in this voltage range became slightly inactive after the initial cycle.

To further investigate the irreversible sodium capacity, capacities of the HCs were deconvoluted into the "slope," "transition," and "plateau" capacity regions (Figure S9d–f, Supporting Information) according to the "adsorption-intercalation–nanopore filling" mechanism.[27a] It is worth noting that the absence of the two well-defined redox peaks (between OCV to 0.1 V vs Na/Na^+) in cyclic voltammogram can be attributed to similar adsorption and intercalation capacities (Figure 5d) and wide storage potential range. According to this mechanism, the "slope" capacity can be attributed to the pseudo-adsorption and defect-adsorption mechanisms. More notably, there was negligible intercalation and nanopore filling capacity changes during the initial three cycles indicating a good reversibility sodium storage mechanism in all HCs (Figure 5d). Among all, HCP exhibited the least changes in the "adsorption" capacity followed by HCT and HC which coincides with the amount of "adsorption" sodiation capacity of HCP, HCT, and HC (≈47.9, 79.6, 87.9 mAh g^{-1}, respectively) and the observation in cyclic voltammogram. Thus, the majority of the irreversible sodium ions in HC and HCT can be attributed to the low reversibility of the "adsorption" capacity as it is associated with a large binding energy which requires large force to remove the Na^+ ions.[12a] It is noteworthy that the HCT exhibited a lower "adsorption" capacity compared to HC, which can be attributed

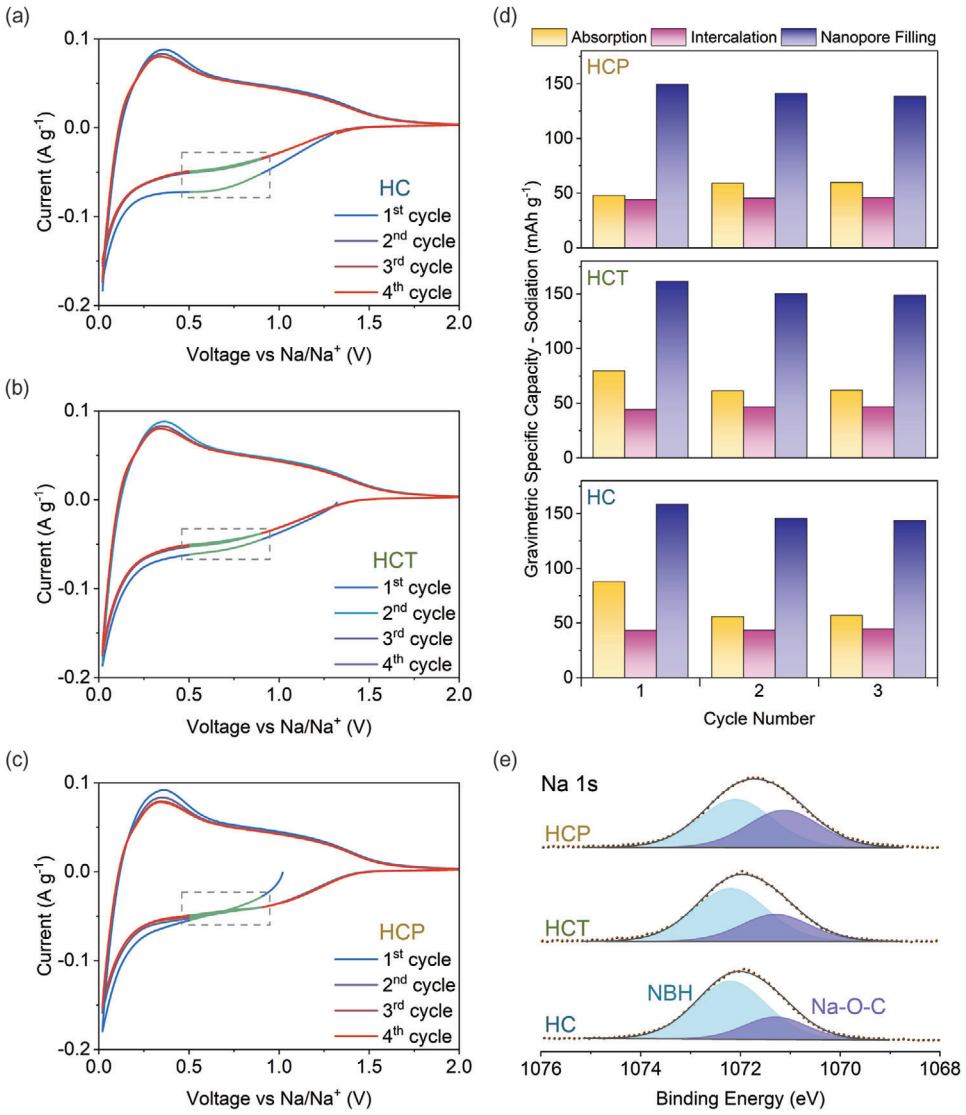

Figure 5. Cyclic voltammogram of a) HC, b) HCT, and c) HCP. d) Initial three cycles sodiation capacity according to the sodium storage mechanism. e) High-resolution Na 1s XPS spectra after the first cycle.

to the higher C_{sp2}:C_{sp3} ratio observed in HCT due to its higher degree of graphitization.[12c]

The Na 1s XPS spectra of all cells after one galvanostatic cycle can be resolved into two peaks at 1072.3 and 1070.9 eV (Figure 5e), which can be attributed to the sodium in NBH electrolyte and Na–O–C group in the HC electrodes, respectively. The presence of Na–O–C was also reported in ex situ XPS of hard carbon after sodiating to the adsorption capacity.[11,21] This observation evidenced that sodium ions that were strongly bound to the oxygen functional groups in hard carbon would lead to irreversible capacity loss. Since intrinsic irreversibility is inevitable due to the structure of HC, presodiation is required to achieve high initial coulomb efficiencies.

The importance of achieving high ICE is further overstated when using a full-cell configuration (AS^3iB) consisting of HC (HCT or HCP), NBH, $Na_{2.25}Y_{0.25}Zr_{0.75}Cl_6$ (NYZC), and $NaCrO_2$ (NCO) as the anode, separator, catholyte, and cathode, respectively. Due to the limited sodium ions inventory provided by NCO, any sodium inventory loss in the initial or subsequent cycles will negatively affect the reversible capacity of the cell. **Figure 6**a shows the potential response of the AS^3iBs during the first cycle at 1/10 C (1 C = 120 mA g^{-1}_{NCO}). Compared to the potential response of Na_9Sn_4||NCO (Figure S10a,b, Supporting Information), the AS^3iBs with HC, HCT, and HCP showed an initial "slope" profile, followed by a potential profile that is like the Na_9Sn_4||NCO half-cell in the later stages of charging. Furthermore, the AS^3iBs had the "hump" between 1.5 to 2.5 V in the initial cycle dQ/dV plots which is absence in Na_9Sn_4||NCO half-cell (Figure S11a–d, Supporting Information). This observation agrees well with the sodiation potential profile of HCs, which consist of slope followed by plateau (Figure 3b). Additionally, the intensity of the "hump" decreased after the initial cycle with the exception for HCP cell indicating the irreversible sodium storage in hard carbon in the initial cycle. Although all cells exhibited

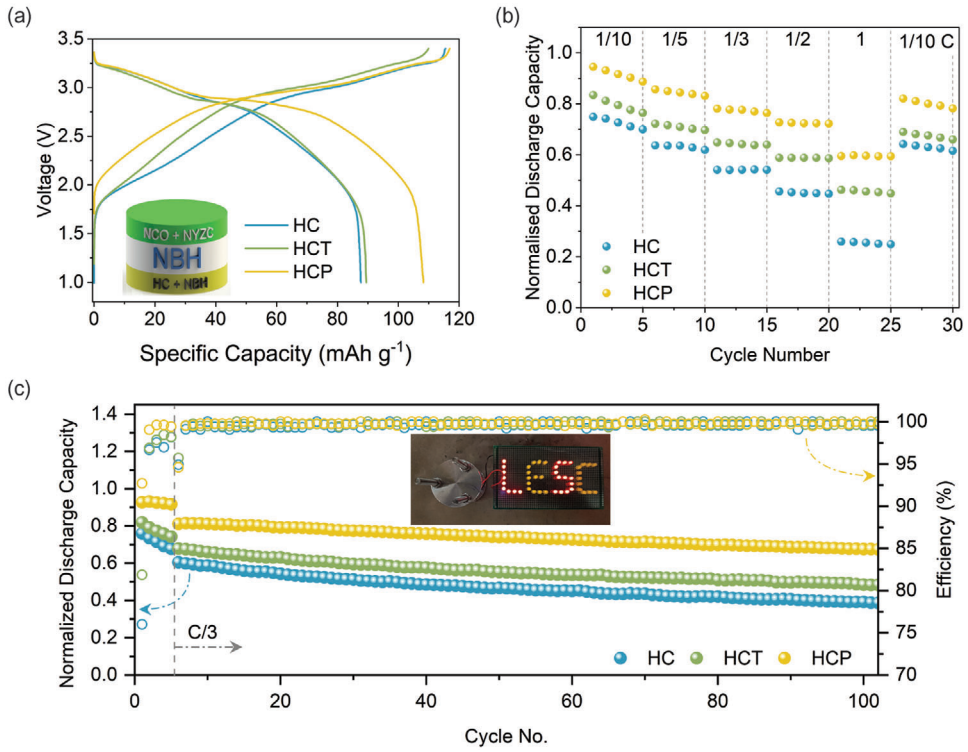

Figure 6. a) Potential response of HCs|NBH|NYZC|NCO AS^{3}iBs in the initial cycle at 1/10 C. b) Reversible discharge capacity at varying current densities. c) Capacity retention of HCs|NBH|NYZC|NCO cell at 1/3 C.

similar charge capacities around 115–120 mAh g^{-1}, the discharge capacity of HC, HCT, and HCP were 86, 91, and 108 mAh g^{-1}, respectively. Accordingly, HC, HCT, and HCP AS^{3}iBs exhibited ICEs of 75.2 ± 0.7%, 82.2 ± 1.1%, and 92.0 ± 2.2%, respectively. This trend agrees well with the ICEs of the half-cells. Additionally, HCP had an initial discharge energy density of 294 Wh kg_{NCO}^{-1} which is higher than HC and HCT (238 and 279 Wh kg_{NCO}^{-1}, respectively). This is due to reduced "slope" capacity in HCP, resulting in a higher average cell voltage, and higher ICE.

Figure 6b shows the normalized reversible capacities of AS^{3}iBs at different current densities and the potential profiles of cells using HC, HCT, and HCP are depicted in Figure S12, Supporting Information. Like the half-cell trend, the HCP delivered the highest reversible capacity compared to HCT and HC. The capacities returned to similar initial capacity when the current density was reduced back to 1/10 C implying that AS^{3}iBs were highly stable at high current densities. It is noteworthy that the Coulombic efficiency of all cells improved to above 98% within the next four cycles at 1/10 C indicating a good reversibility of the cells. Thus, the reversible capacity differences are predominantly caused by initial sodium loss in the first cycle.

The reversibility of the AS^{3}iBs was studied by cycling at 1/10 C for five cycles, which act as the formation cycles, followed by 100 cycles at a 1/3 C (Figure 6c). HCP delivered a higher initial normalized capacity of 0.92 and 0.81 compared to HC (0.76 and 0.60) and HCT (0.82 and 0.68) at 1/10 C and 1/3 C, respectively. It is noteworthy that the HC and HCT cells exhibited a greater increase in overpotential over 100 cycles than that of HCP full-cell (Figure S12, Supporting Information). As a result, HC and HCT had a lower capacity retention of 60.1% and 70.8%, respectively, than HCP (82.3%) after 100 cycles at 1/3 C. Thus, presodiation of the anode is one of the promising strategies to achieve high performance all-solid-state sodium-ion batteries.

3. Conclusion

This study demonstrated that HC is a promising anode candidate in AS^{3}iBs. However, the intrinsic irreversible sodium loss in the HC led to low ICE even when paired with an electrochemically stable solid-state electrolyte. This study explored two strategies to improve the ICE: additional pyrolysis at 1000 °C and presodiation by the thermal decomposition of $NaBH_4$. Thermal treatment of hard carbon was shown to be effective in increasing graphitization and the C_{sp2}:C_{sp3} ratio. The thermal decomposition of $NaBH_4$ produced metallic sodium on the surface of the HC particles, which was shown to be necessary to compensate for the intrinsic irreversible sodium storage sites. Consequently, thermally treated HC improved the ICE from 83% to 90% and the presodiated HC achieved an ICE >99%. Additionally, the half-cells exhibited minimal capacity fading after 600 cycles at 0.5 mA cm^{-2}. More notably, AS^{3}iBs with presodiated HC and NCO as the anode and cathode, respectively, delivered a reversible discharge capacity of 108 mAh g^{-1} at room temperature and an extremely high ICE of 92 ± 2.2%, which is significantly higher than that of HC (75%) and HCT (82%). This work demonstrates significant progress toward enabling practical sodium AS^{3}iBs by utilizing presodiated HC.

4. Experimental Section

Synthesis of NBH: Stoichiometric amount of $Na_2B_{10}H_{10}$ and $Na_2B_{12}H_{12}$ (Boron Specialties LLC) were ball-milled at 500 rpm for 2 h. The as-obtained powder was then dried at 175 °C under vacuum for 48 h. Due to its hydroscopic nature, all operations were conducted in a glovebox with H_2O <1.0 ppm.

Hard Carbon Preparation: The pristine HC (MSE Supplies LLC) was used as received. To study the pyrolysis effect, HC was thermally treated at 1000 °C for 2 h forming HCT. HCP was synthesized by mixing a proportional amount of $NaBH_4$ (Sigma-Aldrich) and HC using a mortar and pestle. Then, the mixture was thermally treated at 650 °C for 3 h in sealed quartz ampoule under vacuum. The amount of $NaBH_4$ added to the HC was calculated according to the capacity loss in the initial cycle.

Material Characterization: XRD was conducted using a Bruker X8-ApexII CCD Sealed Tube diffractometer equipped with a molybdenum Kα radiation ($\lambda = 0.71$ Å) over a 2θ range of 5° to 40°. Samples were sealed in a thin-walled capillary tube to minimize ambient air exposure. Raman spectroscopy was performed using Renishaw inVia Raman Microscope and 532 nm laser source. Due to its air-sensitivity, HCP was sealed on very thin glass slides with Kapton tape in Ar-filled glovebox. XPS was conducted using a Kratos Axis Supra XPS instrument and Al Kα radiation. The data was then analyzed using CasaXPS and was calibrated using the C 1s peak at 284.5 eV. Titration gas chromatography was conducted using Agilent Technologies 7890B to quantify the amount of hydrogen and the amount of metallic sodium was calculated according to Equation (3). SEM images were acquired by an FEI Scios DualBeam Focused ion beam, equipped with an Everhart–Thornley Detector. TEM was performed on a Talos F200X Scanning/Transmission Electron Microscope at 200 kV. HRTEM and HAADF images were collected with a Ceta camera. STEM-EDS/EELS were collected with 4 in-column SDD Super-X detectors and Gatan's Enfinium ER (977) spectrometer with UltraFast DualEELS spectrum, respectively.

$$2Na + 2H_2O \rightarrow 2NaOH + H_2\,(g) \quad (3)$$

Electrochemistry Characterization: Composite HC electrodes were prepared by homogenizing the HC (or HCT/HCP) and NBH with a mass ratio of 70:30 using a mortar and pestle. The half-cell configuration using Na_9Sn_4 as the counter electrode was prepared by compacting NBH (≈60 µm) at 225 MPa. Then, the composite electrode was added on one side and the structure was compact again at 225 MPa. Finally, Na_9Sn_4 was added to the other side of the NBH and the cell was compacted again at 225 MPa. For comparison, different HC composite electrodes (with a HC:NBH ratio of 100:0, 80:20, and 60:40) half-cells were prepared by following similar procedures as described earlier but the weight of composite electrodes varied to have 7 mg of active HC to achieve similar capacity. The AS^3iB (full-cell) configuration included the composite HC (HCT or HCP), NBH, and composite $NaCrO_2$ (NCO) as the anode, electrolyte, and cathode, respectively, with a negative:positive electrode capacity ratio of 1.2. The cathode composite was prepared according to previous work with an NCO:NYZC:C weight ratio 4:5:1.[33] The AS^3iB was compacted with a pressure of 225 MPa. The NCO active material of the electrode was around 6.11 mg cm^{-2}. All capacities were normalized by the initial sodiation capacity of HCs.

CV and electrochemical impedance spectroscopy (EIS) measurements were conducted using a Solartron S1260 impedance analyzer coupled with a Solartron 1287 potentiostat. EIS was conducted in a frequency between 1 MHz to 0.1 Hz at room temperature and with an applied voltage of 10 mV. The EIS of the cell was recorded after resting the cell for at least 3 h. The galvanostatic cycling of the cell was conducted using a Landt battery cycler. The average ICE and OCV were calculated based on four of the similar cells. For the AS^3iBs, the cells were cycled between 1 and 3.4 V. The capacities of the AS^3iBs were normalized by the weight of the NCO in the cathode composite.

Supporting Information

Supporting Information is available from the Wiley Online Library or from the author.

Acknowledgements

J.A.S.O. and G.D. contributed equally to this work. This work was supported by the Shell Global Solutions Inc. (Project No.: 2025754) and the National Science Foundation through the Partnerships for Innovation (PFI) (Grant No.: 2044465). Electron microscopy was performed at the San Diego Nanotechnology Infrastructure (SDNI) of UCSD, a member of the National Nanotechnology Coordinated Infrastructure, which is supported by the National Science Foundation (Grant No.: ECCS-2025752). X-ray photoelectron spectroscopy was performed using facilities in UC Irvine Materials Research Institute (IMRI), which is supported in part by the National Science Foundation through the UC Irvine Materials Research Science and Engineering Center (Grant No.: DMR-2011967) and the National Science Foundation Major Research Instrumentation Program (Grant No.: CHE-1338173). J.A.S.O. is thankful for post-doctorate fellowship support from the Agency of Science, Technology, and Research (A*STAR).

Conflict of Interest

The authors declare no conflict of interest.

Data Availability Statement

The data that support the findings of this study are available from the corresponding author upon reasonable request.

Keywords

all-solid-state batteries, anode materials, hard carbon, presodiation, sodium batteries

Received: March 13, 2023
Revised: April 26, 2023
Published online:

[1] X. Sun, M. Ouyang, H. Hao, *Joule* **2022**, *6*, 1738.
[2] H. S. Hirsh, Y. Li, D. H. S. Tan, M. Zhang, E. Zhao, Y. S. Meng, *Adv. Energy Mater.* **2020**, *10*, 2001274.
[3] a) J. A. S. Oh, L. He, B. Chua, K. Zeng, L. Lu, *Energy Storage Mater.* **2021**, *34*, 28; b) S. Wenzel, T. Leichtweiss, D. A. Weber, J. Sann, W. G. Zeier, J. Janek, *ACS Appl. Mater. Interfaces* **2016**, *8*, 28216.
[4] a) L. Duchêne, R. S. Kühnel, E. Stilp, E. Cuervo Reyes, A. Remhof, H. Hagemann, C. Battaglia, *Energy Environ. Sci.* **2017**, *10*, 2609; b) L. Duchêne, S. Lunghammer, T. Burankova, W.-C. Liao, J. P. Embs, C. Copéret, H. M. R. Wilkening, A. Remhof, H. Hagemann, C. Battaglia, *Chem. Mater.* **2019**, *31*, 3449; c) A. Gigante, L. Duchene, R. Moury, M. Pupier, A. Remhof, H. Hagemann, *ChemSusChem* **2019**, *12*, 4832.
[5] L. Duchene, R. S. Kuhnel, D. Rentsch, A. Remhof, H. Hagemann, C. Battaglia, *Chem. Commun.* **2017**, *53*, 4195.
[6] a) M. Lao, Y. Zhang, W. Luo, Q. Yan, W. Sun, S. X. Dou, *Adv. Mater.* **2017**, *29*, 1700622; b) Z. G. Liu, R. Du, X. X. He, J. C. Wang, Y. Qiao, L. Li, S. L. Chou, *ChemSusChem* **2021**, *14*, 3724; c) T. Perveen, M. Siddiq, N. Shahzad, R. Ihsan, A. Ahmad, M. I. Shahzad, *Renewable Sustainable Energy Rev.* **2020**, *119*, 109549.

[7] a) D. A. Stevens, J. R. Dahn, *J. Electrochem. Soc.* **2000**, *147*, 1271; b) E. Irisarri, A. Ponrouch, M. R. Palacin, *J. Electrochem. Soc.* **2015**, *162*, A2476; c) V. L. Chevrier, G. Ceder, *J. Electrochem. Soc.* **2011**, *158*, A1011.

[8] a) J. Sun, Y. Sun, J. A. S. Oh, Q. Gu, W. Zheng, M. Goh, K. Zeng, Y. Cheng, L. Lu, *J. Energy Chem.* **2021**, *62*, 497; b) M. Zhang, Y. Li, F. Wu, Y. Bai, C. Wu, *Nano Energy* **2021**, *82*, 105738.

[9] a) X. Liu, Y. Tan, T. Liu, W. Wang, C. Li, J. Lu, Y. Sun, *Adv. Funct. Mater.* **2019**, *29*, 1903795; b) E. de la Llave, V. Borgel, K. J. Park, J. Y. Hwang, Y. K. Sun, P. Hartmann, F. F. Chesneau, D. Aurbach, *ACS Appl. Mater. Interfaces* **2016**, *8*, 1867.

[10] S. Komaba, W. Murata, T. Ishikawa, N. Yabuuchi, T. Ozeki, T. Nakayama, A. Ogata, K. Gotoh, K. Fujiwara, *Adv. Funct. Mater.* **2011**, *21*, 3859.

[11] E. Memarzadeh Lotfabad, P. Kalisvaart, A. Kohandehghan, D. Karpuzov, D. Mitlin, *J. Mater. Chem. A* **2014**, *2*, 19685.

[12] a) D. Sun, B. Luo, H. Wang, Y. Tang, X. Ji, L. Wang, *Nano Energy* **2019**, *64*, 103937; b) X. Dou, I. Hasa, D. Saurel, C. Vaalma, L. Wu, D. Buchholz, D. Bresser, S. Komaba, S. Passerini, *Mater. Today* **2019**, *23*, 87; c) L. Xiao, H. Lu, Y. Fang, M. L. Sushko, Y. Cao, X. Ai, H. Yang, J. Liu, *Adv. Energy Mater.* **2018**, *8*, 1703238.

[13] a) D. Dewar, A. M. Glushenkov, *Energy Environ. Sci.* **2021**, *14*, 1380; b) K. Zou, W. Deng, P. Cai, X. Deng, B. Wang, C. Liu, J. Li, H. Hou, G. Zou, X. Ji, *Adv. Funct. Mater.* **2020**, *31*, 2005581.

[14] a) M. Liu, J. Zhang, S. Guo, B. Wang, Y. Shen, X. Ai, H. Yang, J. Qian, *ACS Appl. Mater. Interfaces* **2020**, *12*, 17620; b) G. Zheng, Q. Lin, J. Ma, J. Zhang, Y. B. He, X. Tang, F. Kang, W. Lv, Q. H. Yang, *InfoMat* **2021**, *3*, 1445; c) H. Fang, S. Gao, M. Ren, Y. Huang, F. Cheng, J. Chen, F. Li, *Angew. Chem., Int. Ed. Engl.* **2023**, *62*, 202214717.

[15] a) S. Qiu, L. Xiao, M. L. Sushko, K. S. Han, Y. Shao, M. Yan, X. Liang, L. Mai, J. Feng, Y. Cao, X. Ai, H. Yang, J. Liu, *Adv. Energy Mater.* **2017**, *7*, 1700403; b) S. Alvin, D. Yoon, C. Chandra, H. S. Cahyadi, J.-H. Park, W. Chang, K. Y. Chung, J. Kim, *Carbon* **2019**, *145*, 67.

[16] Y. Cao, L. Xiao, M. L. Sushko, W. Wang, B. Schwenzer, J. Xiao, Z. Nie, L. V. Saraf, Z. Yang, J. Liu, *Nano Lett.* **2012**, *12*, 3783.

[17] H. D. Asfaw, C. W. Tai, M. Valvo, R. Younesi, *Mater. Today Energy* **2020**, *18*, 100505.

[18] a) Z.-l. Zhang, R. Brydson, Z. Aslam, S. Reddy, A. Brown, A. Westwood, B. Rand, *Carbon* **2011**, *49*, 5049; b) H. Lu, F. Ai, Y. Jia, C. Tang, X. Zhang, Y. Huang, H. Yang, Y. Cao, *Small* **2018**, *14*, 1802694.

[19] A. Sadezky, H. Muckenhuber, H. Grothe, R. Niessner, U. Pöschl, *Carbon* **2005**, *43*, 1731.

[20] Y. Chang, X. Sun, M. Ma, C. Mu, P. Li, L. Li, M. Li, A. Nie, J. Xiang, Z. Zhao, J. He, F. Wen, Z. Liu, Y. Tian, *Nano Energy* **2020**, *75*, 104947.

[21] Y. Li, Y.-S. Hu, M.-M. Titirici, L. Chen, X. Huang, *Adv. Energy Mater.* **2016**, *6*, 1600659.

[22] T. Shirasaki, A. Derré, M. Ménétrier, A. Tressaud, S. Flandrois, *Carbon* **2000**, *38*, 1461.

[23] a) A. Barrie, F. J. Street, *J. Electron Spectrosc. Relat. Phenom.* **1975**, *7*, 1; b) Z. Wang, X. Feng, Y. Bai, H. Yang, R. Dong, X. Wang, H. Xu, Q. Wang, H. Li, H. Gao, C. Wu, *Adv. Energy Mater.* **2021**, *11*, 2003854.

[24] Y. Liu, J. S. Xue, T. Zheng, J. R. Dahn, *Carbon* **1996**, *34*, 193.

[25] G. Deysher, Y. T. Chen, B. Sayahpour, S. W. Lin, S. Y. Ham, P. Ridley, A. Cronk, E. A. Wu, D. H. S. Tan, J. M. Doux, J. A. S. Oh, J. Jang, L. H. B. Nguyen, Y. S. Meng, *ACS Appl. Mater. Interfaces* **2022**, *14*, 47706.

[26] J. T. S. Irvine, D. C. Sinclair, A. R. West, *Adv. Mater.* **1990**, *2*, 132.

[27] a) M. Yuan, B. Cao, H. Liu, C. Meng, J. Wu, S. Zhang, A. Li, X. Chen, H. Song, *Chem. Mater.* **2022**, *34*, 3489; b) H. S. Hirsh, B. Sayahpour, A. Shen, W. Li, B. Lu, E. Zhao, M. Zhang, Y. S. Meng, *Energy Storage Mater.* **2021**, *42*, 78.

[28] C. Fang, J. Li, M. Zhang, Y. Zhang, F. Yang, J. Z. Lee, M. H. Lee, J. Alvarado, M. A. Schroeder, Y. Yang, B. Lu, N. Williams, M. Ceja, L. Yang, M. Cai, J. Gu, K. Xu, X. Wang, Y. S. Meng, *Nature* **2019**, *572*, 511.

[29] a) K. Hofmann, R. Gruehn, B. Albert, *Z. Anorg. Allg. Chem.* **2002**, *628*, 2691; b) M. R. Shabetai, Ph.D. Thesis, University of New Orleans, **2022**; c) Z. Li, C. Bommier, Z. S. Chong, Z. Jian, T. W. Surta, X. Wang, Z. Xing, J. C. Neuefeind, W. F. Stickle, M. Dolgos, P. A. Greaney, X. Ji, *Adv. Energy Mater.* **2017**, *7*, 1602894.

[30] Y. Zhang, M. Wu, J. Ma, G. Wei, Y. Ling, R. Zhang, Y. Huang, *ACS Cent. Sci.* **2020**, *6*, 232.

[31] Q. Liu, Z. Hu, W. Li, C. Zou, H. Jin, S. Wang, S. Chou, S.-X. Dou, *Energy Environ. Sci.* **2021**, *14*, 158.

[32] a) K.-l. Hong, L. Qie, R. Zeng, Z.-q. Yi, W. Zhang, D. Wang, W. Yin, C. Wu, Q.-j. Fan, W.-x. Zhang, Y.-h. Huang, *J. Mater. Chem. A* **2014**, *2*, 12733; b) N. Sun, Z. Guan, Y. Liu, Y. Cao, Q. Zhu, H. Liu, Z. Wang, P. Zhang, B. Xu, *Adv. Energy Mater.* **2019**, *9*, 1901351.

[33] R. Phillip, N. L. H. Bao, S. Elias, D. George, C. Yu-Ting, S. Baharak, C. Ashley, H. So-Yeon, O. J. A. Sam, A. W. Erik, H. S. T. Darren, D. Jean-Marie, C. Raphaële, J. Jihyun, M. Y. Shirley, *ChemRxiv* **2022**, https://doi.org/10.26434/chemrxiv-2022-x7llq.